CALPHAD aided design of a crack-free Al-Mg-Si-Ti alloy with high strength: heterogeneous nucleation and eutectic filling during additive manufacturing

Tao Wen, Zhicheng Li, Jianying Wang, Feipeng Yang, Mengzhen Zhu, Yimou Luo, Lijun Zhang, Zhilin Liu, Dong Qiu, Hailin Yang & Shouxun Ji

CALPHAD aided design of a crack-free Al-Mg-Si-Ti alloy with high strength: heterogeneous nucleation and eutectic filling during additive manufacturing

Tao Wen[a], Zhicheng Li[a], Jianying Wang[a], Feipeng Yang[a], Mengzhen Zhu[a], Yimou Luo[a], Lijun Zhang[a], Zhilin Liu[b], Dong Qiu[c], Hailin Yang[a] and Shouxun Ji[d]

[a]State Key Laboratory of Powder Metallurgy, Central South University, Changsha, People's Republic of China; [b]Light Alloy Research Institute, College of Mechanical and Electrical Engineering, Central South University, Changsha, People's Republic of China; [c]Centre for Additive Manufacturing, School of Engineering, RMIT University, Melbourne, Australia; [d]Brunel Centre for Advanced Solidification Technology (BCAST), Brunel University London, Uxbridge, Middlesex, UK

ABSTRACT

The CALPHAD (calculation of phase diagrams) method was applied to facilitate the design of a crack-free Al-Mg-Si-Ti alloy fabricated by laser-powder bed fusion (L-PBF). Calculation and alloy characterisation show that Ti addition at 0.77 wt.% can offer a synergic effect of increasing the heterogeneous nucleation rate and the growth restriction factor (Q) in the initial solidification stage. Meanwhile, the increase of Mg/Si ratio can promote the formation of Al/Mg_2Si eutectics to provide excellent backfilling ability in the final solidification stage. As a result, the experimental Al-Mg-Si-Ti alloy significantly improve the crack susceptibility. Also, the Al-Mg-Si-Ti alloy with dislocation interaction of Al/Mg_2Si eutectics and Al_3Ti particles show an excellent ultimate tensile strength of 447.8 MPa and elongation of 9.1% under as-LPBFed condition.

1. Introduction

Laser-powder-bed fusion (L-PBF), one of the major additive manufacturing (AM) technologies, offers a novel approach to fabricate light weight and highly-integrated parts with high performance through precise layer-by-layer printing process [1–8]. However, the utilisation of L-PBF for fabricating Al-Mg-Si parts, especially for the popular AA6061 alloy, faces significant challenges due to severe hot cracking issues [9–11]. Among there, a high susceptibility to cracking is mainly attributed to several inherent properties, including (*i*) a significant volume contraction induced via high thermal expansion coefficient leads to a high level of residual stress around the coarse column grains, which is highly associated with crack initiation and propagation [12–14]; (*ii*) the formation of long liquid film channels between dendrites, resulting from the wide solidification range (e.g. ~100°C for AA6061 alloy) between the solidus and liquidus temperatures, normally gives rise to vulnerable intergranular regions that are susceptible to the initiation of hot cracks [15–17].

Extensive efforts have been made to mitigate the hot cracks of AA6061 alloy by tuning process parameters [18–22]. In addition to the appropriate laser-energy-related parameters (e.g. laser power and scan speed) [18–20], the adjustable platform preheating temperatures (200 ~500°C) can minimise the thermal gradient and stress during rapid solidification, leading to a significant reduction in hot cracks [21,22]. Nevertheless, it is not feasible to completely prevent the occurrence of hot cracks due to the narrow process windows and the inherent difficulty in eliminating coarse columnar grains, and the excessive platform preheating is also more likely to modify the typical microstructure and deplete Mg/Si from *α*-Al matrix permanently [23]. Meanwhile, the introduction of Al_3(Sc, Zr) via the incorporation of Sc/Zr or agents (e.g. ZrH_2 and YSZ particles) mixed with the pre-alloyed AA6061 powder, has also been proven effective in mitigating hot crack issues through columnar-equiaxed-transition (CET) [23–27]. With an improved printability of the L-PBF AA6061 alloy, the intricate challenges that are involved in unsatisfactory

mechanical response, high cost of Sc/Zr and the requirement and homogenisation control of additional powder processing [1–3], need to be tackled even more thoroughly in the context of large-scale engineering applications. Therefore, much attention should be focused to design and fabricate crack-free L-PBFed Al-Mg-Si alloy with high strength.

Based on the characteristics of crack-prone AA6061 alloy, the incorporation of CALPHAD predication and experimental validation was applied to develop Al-Mg-Si alloys for additive manufacturing. Our strategy is to regulate the composition for cost-effective, to form potent primary dispersoids (L1$_2$-Al$_3$Ti) in the initial stage of solidification via grain refinement and the divorced eutectic Mg$_2$Si in the final stage of solidification for enhancing the cracking-resistance. To this end, the relationship between microstructural characteristics of L-PBFed AA6061/Al-Mg-Si-Ti alloys and the solidification characteristics including solidification sequence, solidification range, eutectic filling and growth restriction factor were systematically investigated. The discussion focuses on the crack elimination and strengthening mechanisms of Al-Mg-Si-Ti alloy.

2. CALPHAD aided design of the Al-Mg-Si-Ti alloy

The AA6061 alloy normally suffers serious cracking during additive manufacturing because of the wide solidification range and the formation of coarse directional columnar grains. The CALPHAD method holds immense potential in facilitating the design of Al alloys [4–6,28,29]. The effects of compositional regulation on the solidification behaviour are calculated via the PanAl2022 thermodynamic database and the results are shown in Figure 1. The solidification sequence of the AA6061 alloy is: L → α-Al → Mg$_2$Si → Si (Figure 1 (a)). The AA6061 alloy exhibits extensive solidification interval of 96.0°C. Furthermore, the *α*-Al phase is directly transformed from liquid when the temperature decreases to 582.2°C, and the prolonged transformation process (L → α-Al: fraction solid f_s reaches up to 92.9%) means that the solidification channel between coarse columnar grains requires more liquid feeding to eliminate the initiation of hot cracks.

To investigate the hot cracking susceptibility of AA6061 with further compositional regulation, the solidification interval, growth restriction factor (Q) and crack susceptibility index (CSI) were calculated based on the Scheil-Gulliver model. Kou model [12] was used to analyse the difference in crack susceptibility after compositional regulation, in which a hot crack criterion

can be calculated as follows:

$$\left\{\frac{d\varepsilon_{local}}{dt} > \sqrt{1-\beta}\frac{d\sqrt{f_s}}{dT}\frac{dT}{dt} + \frac{d}{dz}\left[\left(1-\sqrt{1-\beta}\sqrt{f_s}\right)v_z\right]\right\}_{\sqrt{f_s}\to 1}$$

(1)

where ε_{local}, t, β, T, z, f_s, and v_z represent the local tensile strain in the mushy zone, time, solidification shrinkage, temperature axial direction of columnar dendritic grain, solid fraction and liquid feeding velocity along grain boundary, respectively. An index $|dT/d(f_s)^{1/2}|$ near $f_s^{1/2} = 0.99$ (before completing solidification) is used as a criterion to evaluate the crack susceptibility, which is defined as the *CSI* [12].

Furthermore, the solute addition is highly associated with the constitutional super cooling (ΔT_{CS}) at the front of solid–liquid (S/L) interface, leading to grain refinement [30]. The efficiency of solute to generate ΔT_{CS} is evaluated by the calculation of Q value, which can be expressed by the following equation [31]:

$$Q = \left(\frac{\partial(\Delta T_{cs})}{\partial(f_s)}\right)_{f_s\to 0}$$

(2)

where the f_s and ΔT_{CS} can be obtained by Scheil-Gulliver simulation results. The calculation results of Q value for constrained L → α-Al solidification is presented.

The solidification interval, crack susceptibility index (*CSI*) and growth restriction factor (*Q*) of Al-Mg-Si alloys (Mg: 0–10 wt.% and Si: 0–3 wt.%) are shown in Figure 2. Generally, the narrow solidification interval of the alloys reduced the time that the solid–liquid mushy state existed during solidification, thus reducing the hot crack susceptibility. The solidification interval of Al-Mg-Si alloys gradually decreased with decreasing the Mg content and increasing the Si content, which played an important role in influencing the hot-cracking tendency (Figure 2(a)). Meanwhile, the *CSI* map shown in Figure 2 (b) indicated that a high *CSI* value exceeding 13,000 K was obtained with the composition near AA6061 + 4Mg + 0 Si, AA6061 + 5Mg + 1Si and AA6061 + 7Mg + 2Si alloys, and the composition regulation related to high Mg and Si contents were recommended to induce effective mechanical response (i.e. Mg$_2$Si) and minimise the *CSI* value. Furthermore, the *Q* value of the Al-Mg-Si alloys with various Mg and Si contents varied between 4.3 and 49.7 K (Figure 2(c)), and a large *Q* value was involved in an enhanced solute effect for reducing the grain size. Considering the optimised synergetic effect of low solidification interval, *CSI* and high *Q* value, the addition of Mg and Si into AA6061 alloy was determined as 5 and 2 wt.%, respectively. The correspondingly Al-6Mg-2.5Si alloy exhibited the low solidification interval of 60.7°C, the *CSI* value of 1624.1 K and the high *Q* value
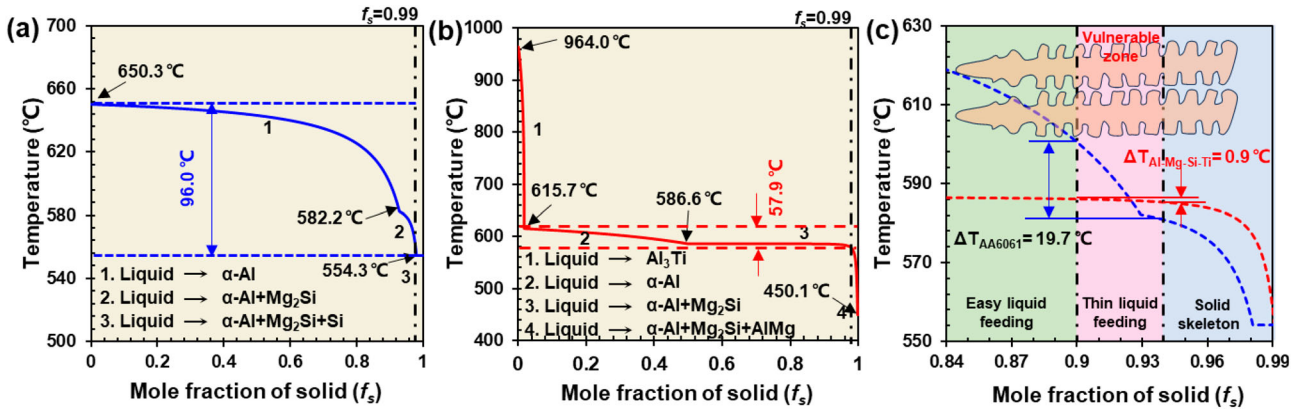
Figure 1. Solidification paths of (a) AA6061 alloy, (b) Al-Mg-Si-Ti alloy calculated using the Scheil-Gulliver model, and (c) enlarged image of (a) and (b) for the final stage of solidification.

of 33.9 K. Moreover, a trace of Ti (0.7 wt.%) was introduced further to obtain superior printability, and the alloy of Al-6Mg-2.5Si-0.7Ti (equivalent to AA6061 + 5Mg + 2Si + 0.7 Ti, denoted as Al-Mg-Si-Ti hereafter) is processed by L-PBF for the features in crack susceptibility, microstructure and mechanical properties.

The solidification sequence of the Al-Mg-Si-Ti alloy is shown in Figure 1(b). It is seen the formation of Al_3Ti phase in the initial solidification stage, and the formation of Mg_2Si phase at a level of $f_s = 49.7\%$ in the solidification of the Al-Mg-Si-Ti alloy. Al_3Ti serves as an effective grain refiner due to its low lattice mismatch with the α-Al matrix and high growth restriction factor. It is also worth noting that the Mg_2Si phase starts to form around $f_s =$ 49.7% in Al-Mg-Si-Ti alloy, in counterpart with a high f_s of 92.9% among AA6061 alloys. Based on Rappaz's theory [32], the cracks are likely to be self-healing due to the formation of a liquid channel with easy liquid when the volume fraction of solid is below 0.9 ($f_s < 0.90$). When f_s is more than 0.94, the solid skeleton structure is continuous and chunky, the continuous liquid channels and films are transformed into separative and isolated liquid drops. There is a vulnerable zone with high hot cracking susceptibility within a single dendrite grain when the solid fraction in the mushy zone is from 0.90 to 0.94 [32]. In the intra-dendritic region, the temperature interval of the vulnerable zone was calculated as 19.7 and 0.9°C for the AA6061 and the Al-Mg-Si-Ti alloys, respectively (Figure 1 (c)). Clearly, the synergetic formation of Al_3Ti and eutectic Mg_2Si phase provided a huge potential in enhancing the hot cracking resistance of the AA6061 alloy.

3. Experimental

3.1. Powder and materials fabrication

The AA6061 and the Al-Mg-Si-Ti pre-alloyed powders were prepared by gas atomisation. The chemical compositions of the AA6061 and the Al-Mg-Si-Ti powders were measured using inductively coupled plasm atomic emission spectrometry (ICAP 7000 Series, Waltham, U.S.A.) and the results are shown in Table 1. The AA6061 and the Al-Mg-Si-Ti powder particles showed a spherical shape with the mean size of 26.8 and 21.8 μm, respectively (Figure 3(a–d)). Meanwhile, EDS mapping confirmed no obvious elemental segregation in the Al-Mg-Si-Ti powders. Prior to L-PBF, the powders were pretreated in a vacuum drying oven 100°C for 8 h. The samples were fabricated by L-PBF machine with an IPG Fibre Laser for microstructural characterisation and mechanical testing. The laser scanning strategy was rotated 67° layer-by-layer (Figure 3(e)), and the processing parameters were optimised as follows to minimise the defects: the laser powder (P) of 310 W, the scan speed (v) of 1000 mm/s, the hatch spacing (h) of 0.1 mm, and layer thickness (t) of 0.03 mm. The samples were built on a substrate plate of AlSi10Mg alloy. The size of cubic samples and cuboid samples were 10 mm × 10 mm × 10 mm and 80 mm × 10 mm × 10 mm, respectively. The dog-bone-shaped samples for testing the mechanical properties with a gauge length of 15 mm and a cross-section of 4 × 2 mm², as shown in Figure 3(f).

3.2. Microstructural characterisation and mechanical properties testing

The surface defects of samples under different conditions were characterised via Leica DM4000M optical microscope (OM). The phase constituent of samples was identified using X-ray diffraction with Cu $K\alpha$ radiation (XRD, Rigaku X-2000). Microstructural characteristics were measured using a scanning electron microscope (SEM, Quanta 250 FEG). The etchant was Keller's solution. The grain size and grain orientation
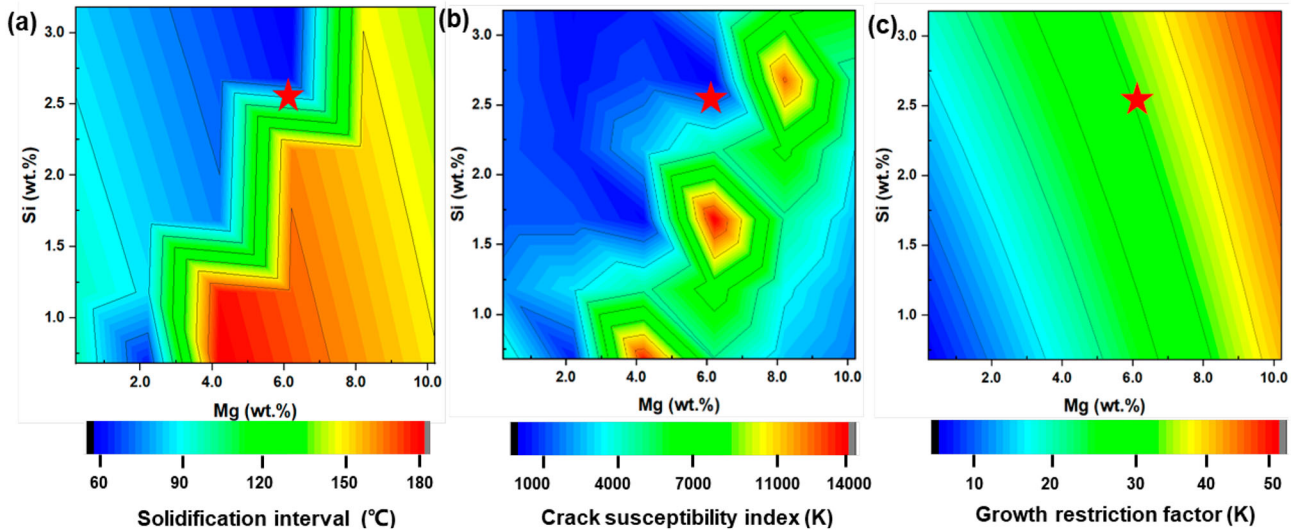
Figure 2. (a) Solidification interval maps calculated using the Scheil-Gulliver model, (b) crack susceptibility index (*CSI*) maps, and (c) growth restriction factor (*Q*) maps in the Al-Mg-Si alloy.

were characterised using an electron backscattered diffraction (EBSD, Helios NaboLab G3 UC). Furthermore, the detailed microstructural characteristics were conducted using a transmission electron microscope (TEM, Talos F200X). TEM samples were prepared by a precision ion polishing system (PIPS, Gatan691) at a voltage of 5 kV and an incident angle of 3~8°. Uniaxial tensile tests were performed using a testing system (MTS, Alliance RT30) with an engineering strain rate of 1×10^{-3} s^{-1} at room temperature (RT). The reported tensile data were the average of three measurements.

4. Results

4.1. Microstructural characteristics

In consistent with the calculation results in Figures 1 and 2, the microstructural characteristics shown in Figure 4 confirmed that the Al-Mg-Si-Ti alloy exhibited high printability, compared with the AA6061 alloy. The Al-Mg-Si-Ti alloy showed a high relative density of 99.8% with a trace of pores (Figure 4(e)). However, the cracks with the length in millimetre scale were parallel to the building direction for the AA6061 alloy, which also propagated along the horizontal direction. Similar to the previous studies [4–6,33,34], the occurrence of hot

cracks in the AA6061 alloy could not be fully eliminated. EBSD map of Figure 4(b) further demonstrated that the coarse columnar grains of AA6061 alloy with a mean size of 100.2 μm grew epitaxially along the building direction, which terminated at a width of 20~100 μm and a length up to hundreds of micron metres. Also, the cracks distributed along the coarse columnar grain boundaries and span over multiple layers. Inverse pole figure and pole figure (IPF/PF) of the AA6061 alloy further revealed that the intersection of cracks and columnar grains had a strong [001] texture with the peak texture intensity of 16.0 in Figure 4(c), while the Al-Mg-Si-Ti alloy was composed of the refined equiaxed grain (4.6 μm) with the random crystallographic texture (Figure 4(g)). Referring to kernel average misorientation (KAM) map in Figure 4(d), a continuous columnar grain with high strain concentration around the crack areas favours the cracking initiation and propagation in the L-PBFed AA6061 alloy. In contrast, the Al-Mg-Si-Ti alloy delivered a uniform misorientation distribution with low value (Figure 4(h)).

The detailed microstructural differences of solidification microstructure between L-PBFed AA6061 and Al-Mg-Si-Ti alloys along the building direction were characterised by SEM. Similar to EBSD results in Figure 4(b), the cracks were normally initiated and propagated along the grain boundaries of the AA6061 alloy that contained irregular Mg$_2$Si particles. In comparison, a typical hierarchical microstructure in the L-PBFed Al-Mg-Si-Ti alloy was composed of the heat affected zone (HAZ), melting pool (MP) coarse zone and MP fine zone (Figure 4(l)), where the equiaxed and columnar structure boundaries were decorated with Mg$_2$Si eutectics that were precipitated along the α-Al grain boundaries

Table 1. Chemical compositions of the AA6061 and the Al-Mg-Si-Ti alloy measured by ICP-AES (wt.%).

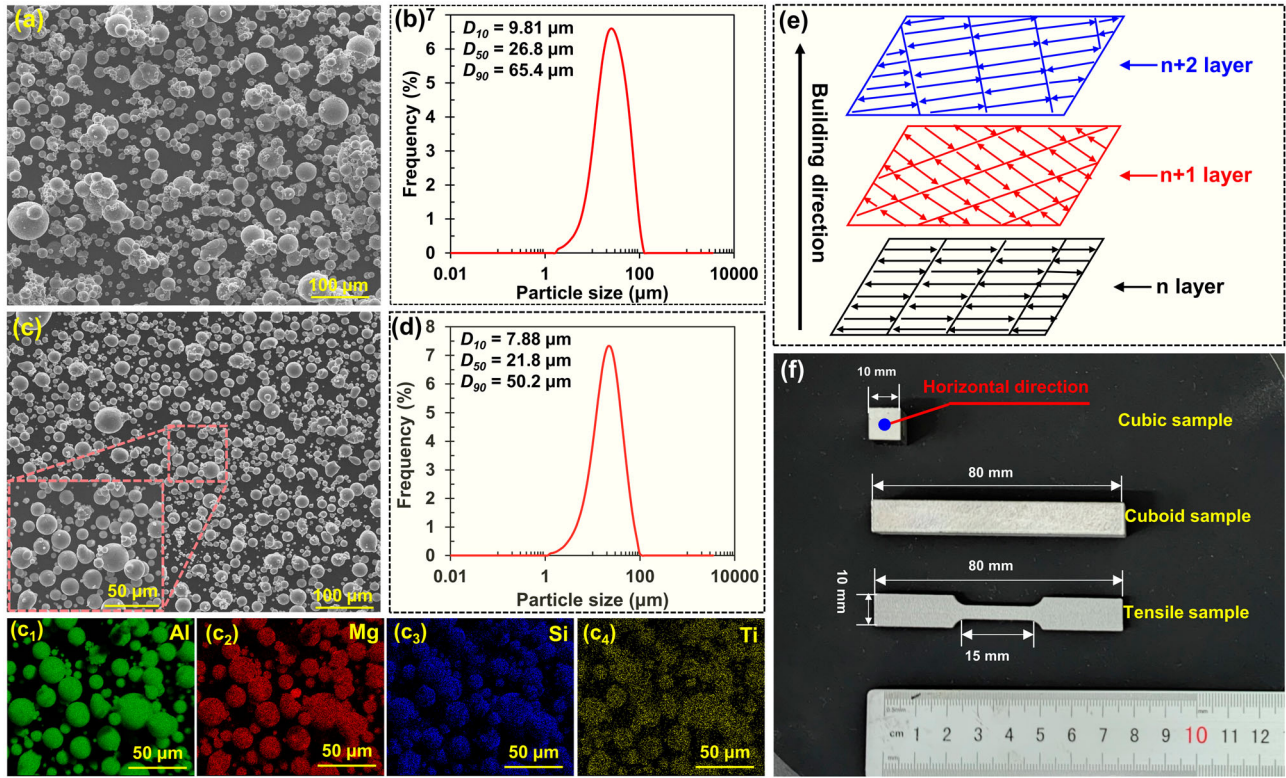| Alloy	Mg	Si	Ti	Cu	Others	Al
AA6061 powder	1.21	0.68	/	0.13	<0.08	Bal.
L-PBFAA6061	1.15	0.63	/	0.11	<0.08	Bal.
Al-Mg-Si-Ti powder	6.23	2.31	0.77	0.09	<0.08	Bal.
L-PBF Al-Mg-Si-Ti	5.85	2.25	0.75	0.08	<0.08	Bal.

Figure 3. Characterisation of pre-alloyed powders including powder particle morphology, particle size distribution and EDS mapping, (a, b) AA6061, (c, d) Al-Mg-Si-Ti, (e) schematic of the scanning strategy during L-PBF, (f) the cubic, cuboid samples; and the detailed dimension of dog-bone-shaped tensile samples.

(Figure 4(m)), and the columnar grains also grew epitaxially along the thermal gradient and preferred orientation (Figure 4(n)). Furthermore, TEM analysis in Figure 5 suggested that the introduction of Al_3Ti particles and Mg_2Si eutectics was highly associated with the excellent printability of the L-PBFed Al-Mg-Si-Ti alloy. HADDF-STEM image and EDS maps (Figure 5(a, a_1–a_4)) confirmed that Mg and Si elements were enriched around the cellular structure boundaries, indicating that the formation of Mg_2Si eutectics. The partial solid solution of Mg, Si, and Ti within Mg_2Si eutectics was also likely to enlarge ΔT_{CS} in front of the solid–liquid interface, which played an important role in grain refinement [13,29]. Meanwhile, the interaction between dislocations and Mg_2Si eutectic was illustrated in Figure 5(b), and the Al/Mg_2Si interface exhibited a coherent orientation relationship (OR) with $(\bar{1}1\bar{1})_{\alpha\text{-Al}}//(202)_{Mg2Si}$, $[001]_{\alpha\text{-Al}}//[\bar{1}11]_{Mg2Si}$ (SAED pattern of Figure 5(a)). Mg_2Si phase was coherent with the α-Al matrix along the $[\bar{1}11]$ direction, with an interplanar spacing of 0.239 nm for the $(11\bar{1})_{Al}$ plane of α-Al matrix and 0.223 nm for the $(202)_{Mg2Si}$ plane of the Mg_2Si phase (Figure 5(e_1, e_2)). It is also seen that the formation of cubic Ti-enriched particles within α-Al matrix exhibited a typical $L1_2$-Al_3Ti lattice structure, as verified by Figure 5(c_1–c_4, d). The α-Al matrix and $L1_2$-Al_3Ti particles showed a

coherent OR with $[001]_{\alpha\text{-Al}}//[001]_{L12\text{-Al3Ti}}$, and the interplanar distances calculated via inverse Fast Fourier Transform (IFFT) images indicated that the (020) interplanar spacing of α-Al matrix and $L1_2$-Al_3Ti was 0.203 and 0.197 nm, respectively. Meanwhile, IFFT image of interface marked by the blue dashed line in Figure 5(g) demonstrated a fully coherent interface between these two phases.

4.2. Mechanical properties

The engineering stress–strain curves of the L-PBF AA6061 and the Al-Mg-Si-Ti alloys are shown in Figure 6(a), and the corresponding yield strength (YS), ultimate tensile strength (UTS) and elongation (El) are summarised in Table 2. The L-PBFed AA6061 alloy exhibited almost no bearing capacity with a UTS of 54.5 MPa and an El of 0.1%, and the fracture morphology exhibited a typical brittle delamination fracture with the existence of cracks and pores (Figure 6(c, d)), which was consistent with the fractography of other crack-prone Al alloys [13,33,34]. In contrast, the Al-Mg-Si-Ti alloy possessed a high YS of 362.4 MPa, UTS of 447.8 MPa and El of 9.1%, preserving an excellent synergy of strength and ductility. The fractured morphology in Figure 6(e, f) signified the existence of a typical ductile fracture
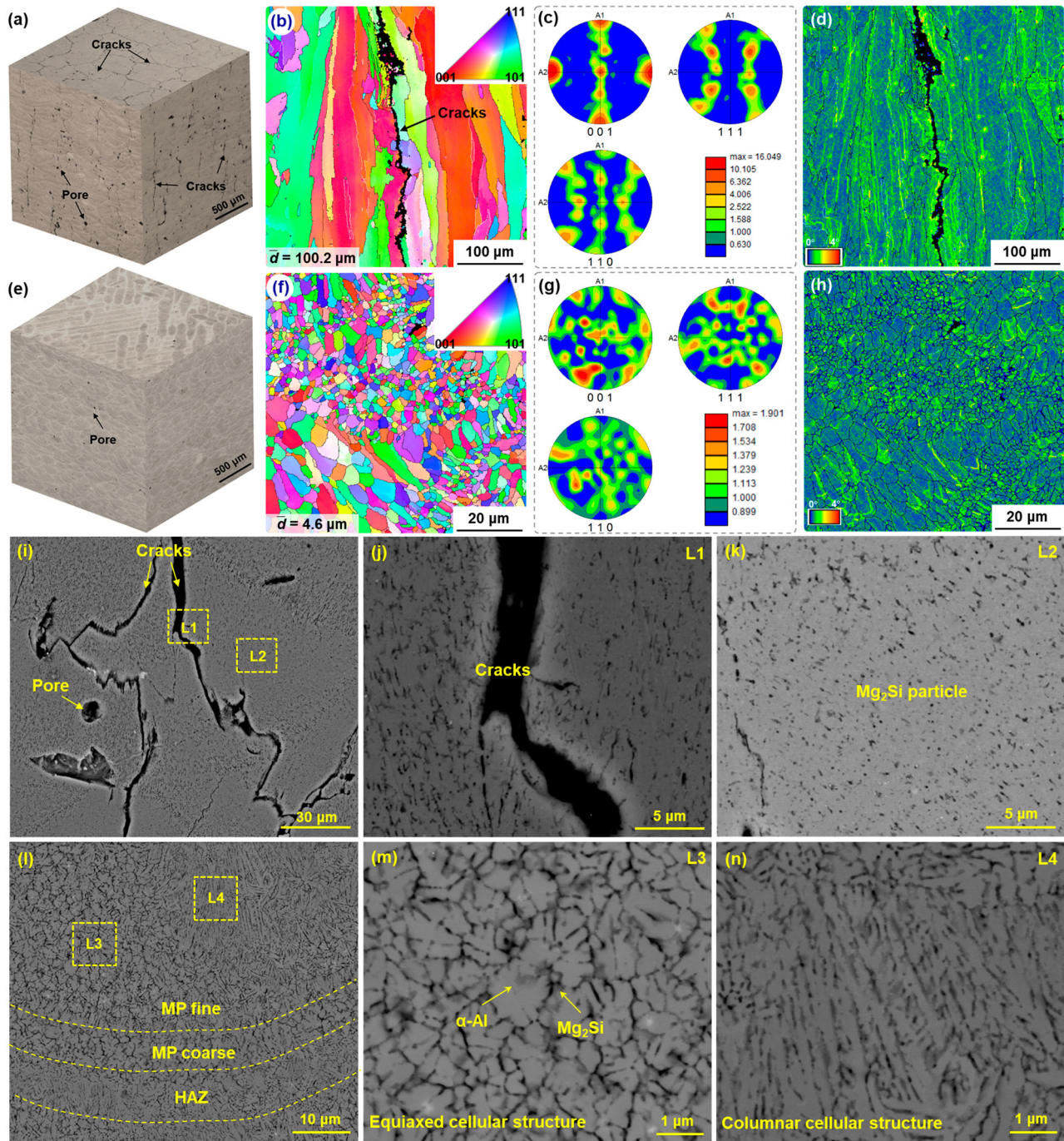
Figure 4. OM images of (a) the AA6061 and (e) the Al-Mg-Si-Ti alloys taken from the XY, YZ and XZ planes; EBSD-IPF maps, grain size distribution, pole figures and KAM image along the build direction: (b-d) the AA6061 alloy; (f-h) the Al-Mg-Si-Ti alloy; Typical solidification microstructure of (i-k) the AA6061 alloy, (l-n) the Al-Mg-Si-Ti alloy.

mode with dimples. Figure 6(b) summarises the mechanical properties of L-PBFed Al-Mg-Si-Ti alloy and conventionally manufactured AA6601 (cast and wrought) [16,35], L-PBFed AA6061 alloy with heated build plate [22,36], AA6061 + Zr/Sc [23,24] and Al–Si-Mg alloys [37–42]. It can be seen that the Al-Mg-Si-Ti alloy exhibited a competitive strength-ductility synergy compared to other Al alloys.

5. Discussion

5.1. Crack elimination mechanisms

5.1.1. The potent primary particles/solutes for grain refinement in the initial stage of solidification

The grain refinement is important to prevent hot cracks during L-PBF and improve mechanical properties. The

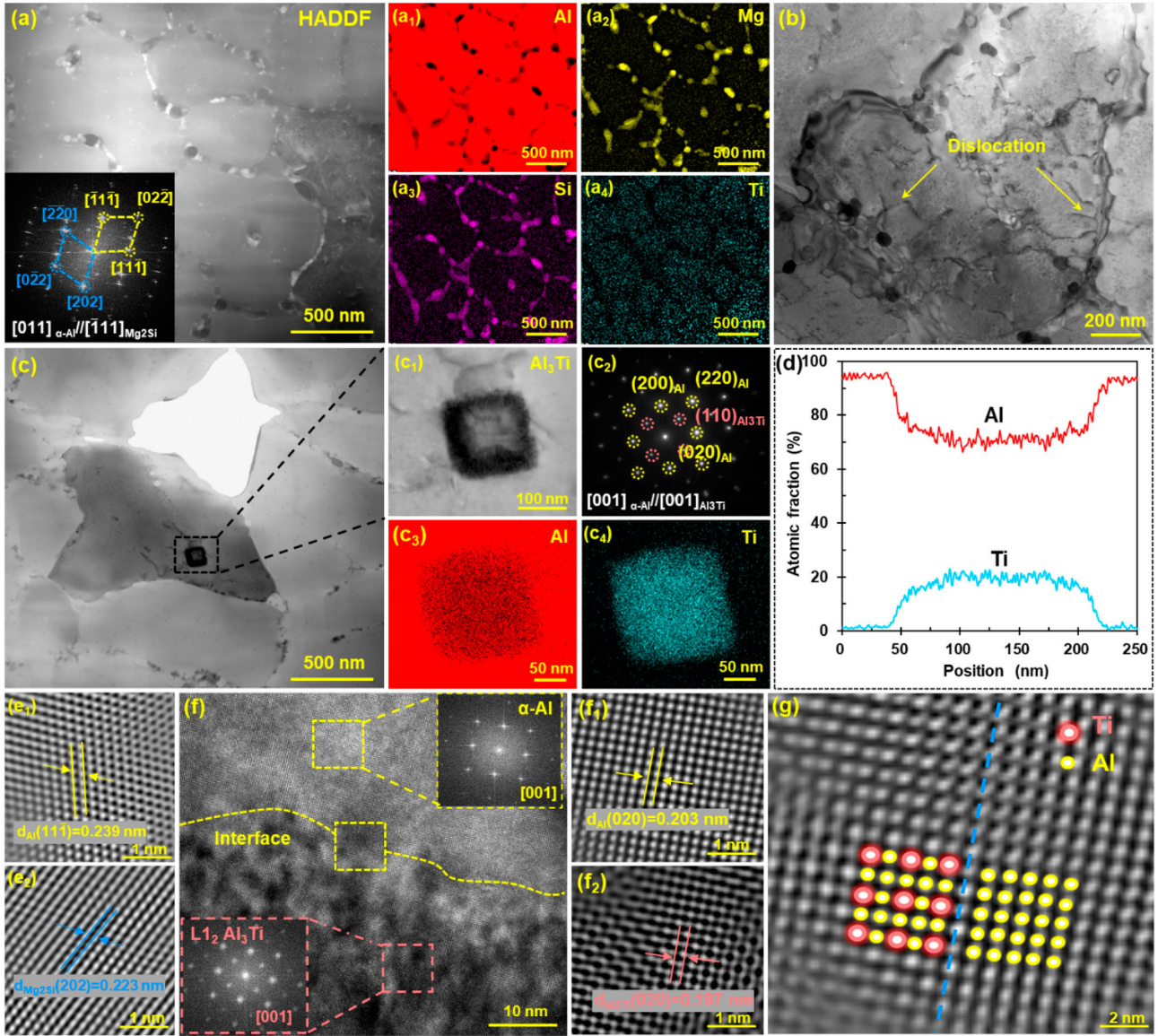**Figure 5.** (a) HAADF-STEM image of L-PBFed Al-Mg-Si-Ti alloy and (a_1-a_4) EDS maps of Al, Mg, Si, and Ti elements; (b) the interaction between the dislocations in Mg_2Si eutectics; (c) BF-TEM micrographs of α-Al matrix containing Al_3Ti particles; (c_2) SAED pattern of $L1_2$-Al_3Ti; (c_3,c_4,d) EDS mapping corresponding the (c_1); (e_1, e_2) IFFT patterns of α-Al matrix and Mg_2Si selected in (a); (f) HR-TEM of the α-Al/ $L1_2$-Al_3Ti interface and (f_1, f_2) IFFT patterns of the α-Al and $L1_2$-Al_3Ti selected in (f); (g) IFFT image of the interface marked by the blue dashed line in (f). Note: the region characterised by TEM is located in the centre of the melt pool.

severe solidification shrinkage involved in the printing of AA6061 alloy tends to trigger the formation of thermal tearing crack (Figure 7(a)). In contrast, the Al-Mg-Si-Ti alloy is mainly featured by fine equiaxed grains. The mechanisms of grain refinement for L-PBF, typically, include (*i*) heterogeneous nucleation and (*ii*) growth restriction effects (Figure 7(b)). The primary Al_3Ti particles precipitated from liquid tend to facilitate the nucleation of α-Al grains because of their low lattice mismatch with the α-Al matrix and high thermodynamic stability [43]. It is noted that the high cooling rate during L-PBF provides favourable conditions for such metastable $L1_2$-Al_3Ti nanoparticles, which are difficult to achieve in

conventional casting methods. The *in-situ* $L1_2$-Al_3Ti particle distributed within the grains exhibits a coherent interface with the α-Al matrix (Figure 5), providing direct evidence that $L1_2$-Al_3Ti particles act as strong nucleants and play a critical role in promoting columnar-to-equiaxed transition (CET). In addition to nucleants, the growth restriction effects are also important for grain refinement. The grain refinement induced via solute addition is highly associated with ΔT_{CS} at the front of S/L interface [44]. The addition of Mg, Si and Ti element can effectively enhance *Q* value (41.2 K), which means that solutes among in the Al-Mg-Si-Ti alloy also exert a positive influence in promoting grain refinement.
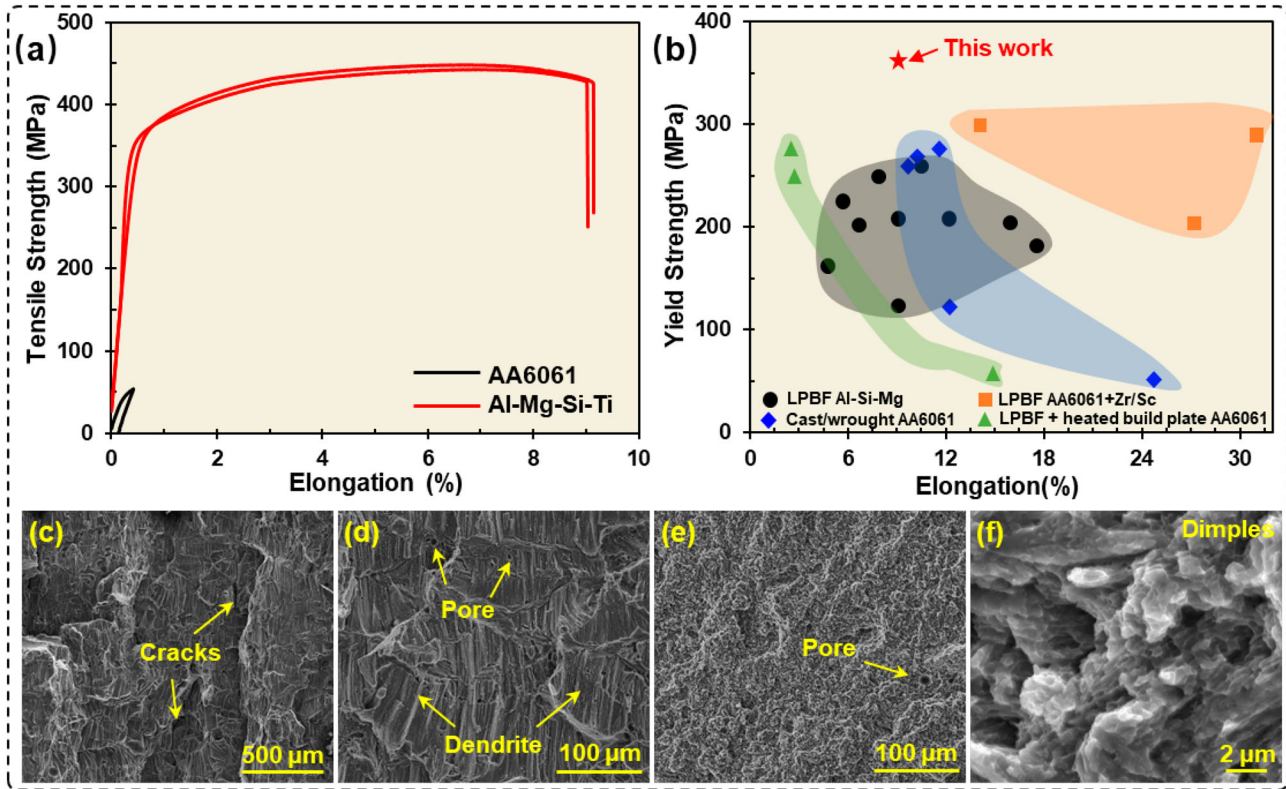
Figure 6. (a) Engineering stress-strain curves of L-PBFed AA6061 and Al-Mg-Si-Ti alloys; (b) a comparison of mechanical properties with the conventionally manufactured AA6601 (cast and wrought), L-PBFed AA6061 with heated build plate, AA6061 + Zr/Sc and Al-Si-Mg; (c, d) fracture morphology of the L-PBFed AA6061 alloy; (e, f) fracture morphology of the L-PBFed Al-Mg-Si-Ti alloy.

It is also mentioned that the stress concentration is prone to occur at the adjacent coarse columnar grains, which is related to the initiation of cracks due to solidification and thermal shrinkage. The equiaxed grains are more likely to accommodate the thermal stress and offer more tortuous crack paths in the counterpart with the flat boundaries of coarse columnar grains, thus preventing crack initiation between adjacent grains and inhibiting the cracks propagation further [16,28]. Moreover, the fine equiaxed grains normally improve the critical stress required for the initiation of hot cracks by offering a higher number density of grain boundaries per unit volume, in contrast to the coarse columnar grains. In this work, the critical stress (σ_c) can be estimated as follows [4–6]:

$$\sigma_c = \frac{8\gamma}{\sqrt{3}d}\left(\frac{f_s^M}{1-f_s^M}\right) \qquad (3)$$

Table 2. Mechanical properties of the L-PBFed AA6061 and Al-Mg-Si-Ti alloys.

Condition	YS (MPa)	UTS (MPa)	El (%)
AA6061	53.4 ± 3	54.5 ± 4	0.1 ± 0.1
Al-Mg-Si-Ti	362.4 ± 4	447.8 ± 6	9.1 ± 0.2

where γ is the liquid surface tension, set to 0.91 and 0.87 N/m based on the JMatPro software for AA6061 and Al-Mg-Si-Ti alloys, respectively. d is the grain size (columnar grains and equiaxed grains are grain width average grains size, respectively). f_s represents the solid fraction in the final solidification stage. M is the microstructure parameter, 1/3 for columnar grains and 1/2 for equiaxed grains. Correspondingly, the calculated results shown in Figure 7(c) further reveal that the refined equiaxed microstructure in the Al-Mg-Si-Ti alloy exhibits much higher critical stress to cracks compared with the AA6061 alloy during final solidification stage (f_s from 0.9 to 0.98).

5.1.2. Eutectics backfilling in the final stage of solidification

Apart from grain refinement, the occurrence of hot cracks is also closely related to the liquid backfilling ability in the final stage of solidification. The various factors that contain grain separation effects caused by solidification and thermal shrinkage strain, grain growth, and liquid backfilling can be taken into account according to Kou's criterion. Although the AA6061 alloy with a low content of Mg, Si delivers a potential in forming a series of eutectic phase (e.g.
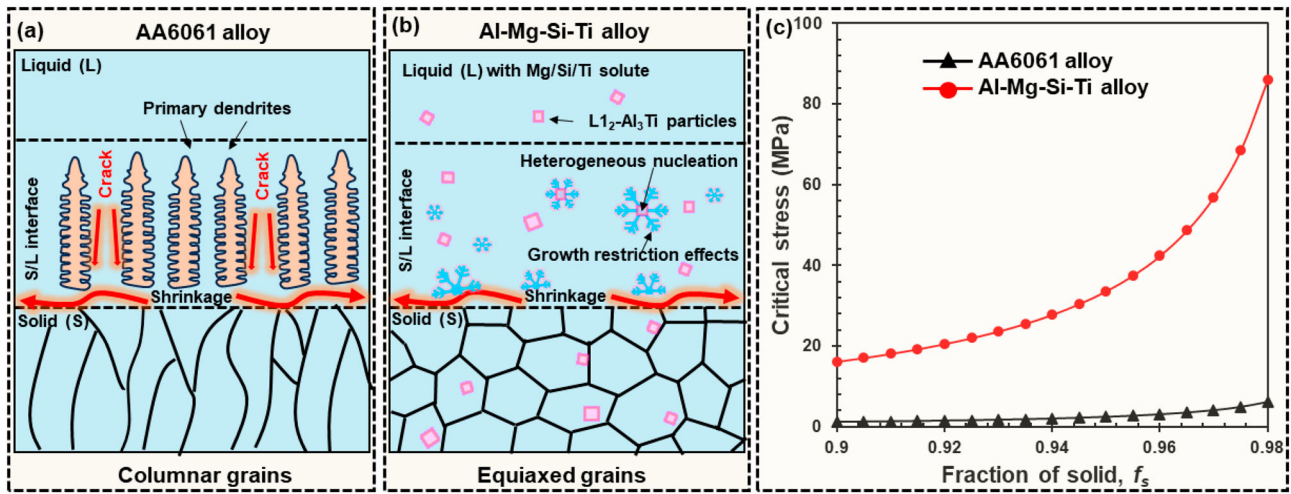
Figure 7. (a) Schematic of the columnar grains and cracks in the L-PBF AA6061 alloy; (b) Schematic of the synergistic grain-refining mechanisms including heterogenous nucleation and growth restriction effects in the L-PBF Al-Mg-Si-Ti alloy; (c) Calculated critical hot cracking stress in the AA6061 and Al-Mg-Si-Ti alloy at the final stage of solidification.

Mg_2Si, Si) during the final stage of solidification, their low content (less than 8%, Figure 1(a)) in the molten pool is depleted with rapid growth of the primary dendrites. Therefore, the liquid phase does not have enough time to move to bottom areas through narrow channels between neighbouring dendrites, which promotes the formation of cracks that propagate over multiple melting pool boundaries. A high alloying content (Mg and Si) in the CALPHAD aided design Al-Mg-Si-Ti alloy brings the increased fraction of Mg_2Si eutectics (Figure 1(b)). Consequently, Al-Mg-Si-Ti alloy shows a lower *CSI* of 1505.2 K than the AA6061 alloy (4472.0 K), delivering better crack resistance. Therefore, the refined microstructure of the Al-Mg-Si-Ti alloy that contains a high number density of Mg_2Si eutectics could enhance liquid backfilling ability and accommodate thermal stresses arising during solidification [45,46], it is one of the critical contribution factors for the elimination of hot cracks in the present study.

5.2. The relationship between microstructural characteristics and strength enhancement

A schematic diagram for the comparison of microstructural characteristics in the L-PBF AA6061 and Al-Mg-Si-Ti alloys is shown in Figure 8. The rapid solidification with large temperature gradient ($G > 10^5$ °C/m) and high cooling rate (T: $10^5 \sim 10^6$ °C/s) during L-PBF process enable the formation of non-equilibrium microstructure in Al alloys [47,48]. The L-PBF AA6061 alloy contains a high number density of hot cracks that form and propagate over multiple melting pool boundaries, and the absence of nucleant sites as well as a trace of

uniformly distributed Mg_2Si particles deliver poor grain refinement and eutectic filling abilities (Figure 8(a–c)). The coarse columnar grains with high concentration stress are more likely to promote the initiation of the cracks under loading [45], smooth crack channels along the large dendrite boundaries are conducive to crack propagation further and a poor bearing capacity (Figure 6(a)). With compositional regulation, the crack-free L-PBF Al-Mg-Si-Ti alloy with only a few pores is mainly featured by Mg_2Si eutectics (Figure 4(l)). It is worth nothing that the specific large temperature gradient and heat accumulation results in a unique cellular structure arrangement, as shown in Figure 8(e). In general, the growth of cellular structure is mainly determined by two factors: cooling rate and compositional regulation (solidification rate and temperature gradient in front of the solidification interface) [49]. Firstly, the surface growth of eutectic phases tends to be transformed into non-faceted growth with the increase of supercooling. The Mg_2Si eutectic are featured by lamella, rod and flake structures in traditional castings [50], while the divorced eutectic Mg_2Si is prone to form in L-PBF Al-Mg-Si alloys (Figure 5(a)). Secondly, the solute segregation (i.e. Mg, Si and Ti) with distinct partition coefficients alters the degree of constitutional supercooling in front of the solidification interface, which exerts a great effect on the transformation from planar/cells/dendrites/cells/planar to the morphology of the S/L interface. The growth of eutectics also depends on the exchange of solute atoms between eutectic phase [51]. With the precipitation of Al_3Ti particles within the liquid, α-Al matrix prefers to nucleate from liquid solution containing high Mg, Si and Ti solutes during the solidification; and then Mg_2Si phase
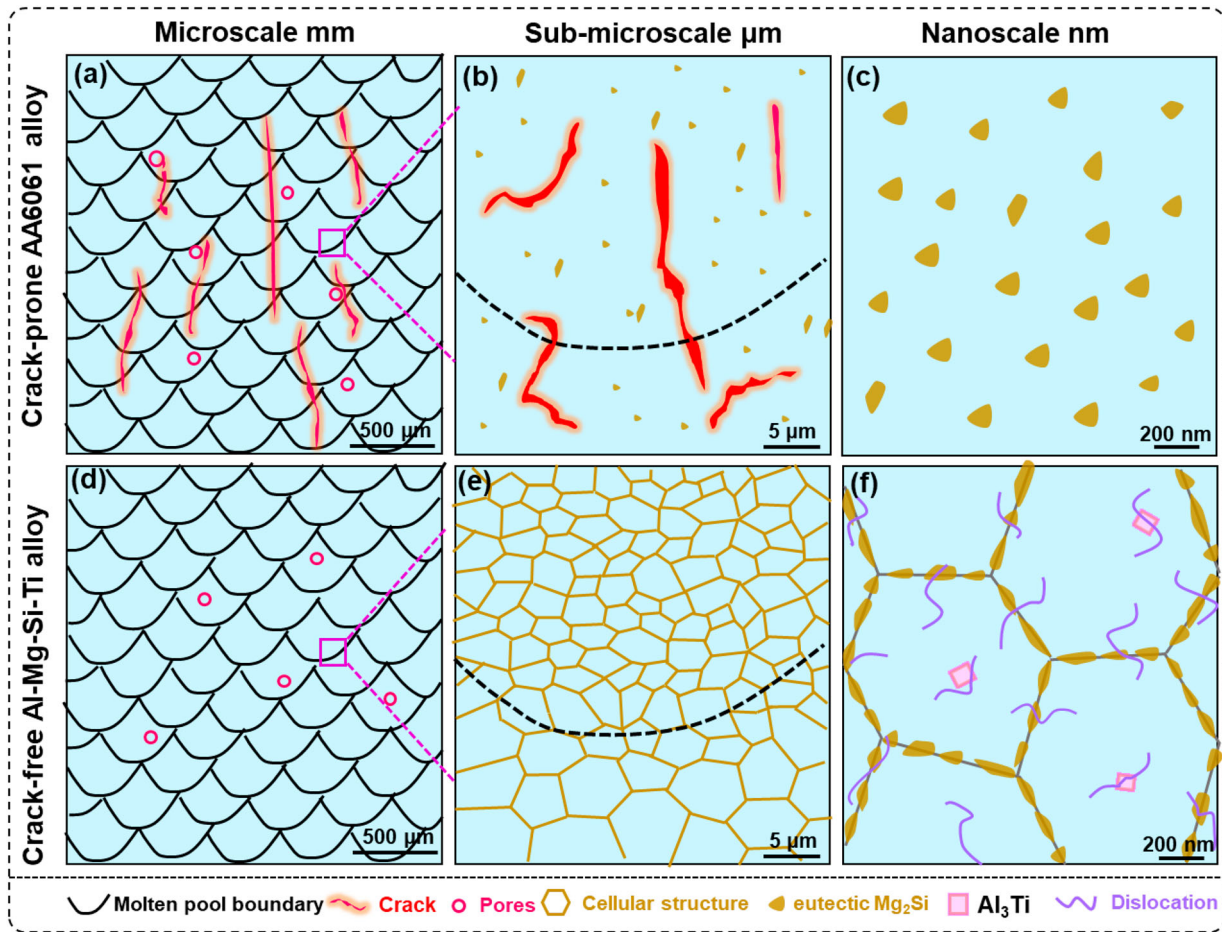
Figure 8. Schematic diagram of the microstructure evolution during solidification: (a-c) AA6061 alloy; (d-f) Al-Mg-Si-Ti alloy.

nucleates and grows around the primary α-Al phase, leading to the formation of Al/Mg$_2$Si eutectics (Figure 8(e–f)).

The L-PBFed Al-Mg-Si-Ti alloy exhibits a unique hierarchical microstructure characteristic that contains micrometre-sized fine α-Al grain, sub-micrometre-sized eutectic Mg$_2$Si cellular structure, nanosized precipitates and solutes, and a high number density dislocation via L-PBF process, which is highly associated with the characteristics of melt pools. Correspondingly, the excellent mechanical properties of Al-Mg-Si-Ti alloy are primarily attributed to the typical hierarchical microstructure: (*i*) the fine α-Al grains (4.6 μm) induced via a combination of heterogeneous nucleation and high growth restriction effect led to a superior grain boundary strengthening; (*ii*) the refined Al/Mg$_2$Si eutectics (∼0.86 μm) deliver a synergetic effect of dislocation storage as well as an effective pining action to dislocation movement, which is conducive to the precipitation strengthening; (*iii*) the solid solubility of element (Mg, Si and Ti) is greatly improved due to the extremely high cooling rate in L-PBF process, which benefits to the solid solution strengthening; (*iv*) The

strength enhancement is also resulted from a high density of dislocations, which arise due to the high strain and thermal contraction stress caused by rapid solidification during L-PBF process. In order to get insights effect of non-equilibrium microstructure on mechanical properties further, the potential strengthening mechanisms are quantitatively evaluated. According to composition regulation, the strength improvement is mainly attributed from fine grains strengthening caused by Ti addition and precipitation strengthening caused by Mg/Si element addition. The detailed calculation data is provided in the supplementary material.

5. Conclusions

In the present study, CALPHAD was used to aid the design of Al-Mg-Si-Ti alloy with high strength and free of cracks was successfully fabricated by L-PBF via tuning solidification characteristics. The crack elimination mechanisms, microstructural evolution and mechanical properties were systematically investigated. The conclusions can be summarised as follow:

(1) The AA6061 alloy shows poor processability, prone to cracking and resulting in low density of 97.3% in the L-PBFed samples. The Al-Mg-Si-Ti alloy presents superior processability, free of cracking and high density of 99.8%. Compared with the coarse columnar microstructure of L-PBFed AA6061 alloy, the L-PBFed Al-Mg-Si-Ti alloy is mainly featured by the refined hierarchical microstructure that contains micro-sized fine α-Al grains, sub-micro-sized eutectic Mg_2Si eutectics, nanosized precipitates/solutes, and a high number density of dislocation.

(2) The crack elimination mechanisms are mainly attributed to a synergic effect of the potent primary particles/solutes in the initial stage of solidification for promoting the grain refinement and eutectics backfilling in the final stage of solidification. Correspondingly, the L-PBFed AA6061 alloy exhibits poor bearing capacity, and the trade-off in mechanical properties between strength and ductility (the UTS of 447.8 MPa and the El of 9.1%) is obtained in the L-PBFed Al-Mg-Si-Ti alloy. Strengthening in the L-PBFed Al-Mg-Si-Ti alloys mainly results from fine α-Al grains, supersaturated solid solutions and the interaction between Al/Mg_2Si eutectics with dislocations.

Funding

Data availability statement

Data will be made available on request.

Credit authorship contribution statement

Tao Wen: Experiments, data collection and analysis, writing – original draft. **Zhicheng Li:** Experiments and data analysis, writing – review. **Jianying Wang:** Experiments and data collection, writing – review & editing, results review. **Feipeng Yang:** Experiments and data analysis. **Mengzhen Zhu:** Conceptualisation and investigation. **Yimou Luo:** Conceptualisation and investigation. **Lijun Zhang:** Conceptualisation, writing – review & editing. **Zhilin Liu:** Conceptualisation, writing – review & editing, supervision. **Hailin Yang:** Conceptualisation, funding acquisition, project management, supervision, writing – editing & review. **Shouxun Ji:** Conceptualisation, results review, writing – editing & review.

References

[1] Jandaghi MR, Pouraliakbar H, Shim SH, et al. In-situ alloying of stainless steel 316L by co-inoculation of Ti and Mn using LPBF additive manufacturing: microstructural evolution and mechanical properties. Mater Sci Eng A. 2022a;857:144114.

[2] Jandaghi MR, Pouraliakbar H, Fallah V, et al. Additive manufacturing of nano-oxide decorated AlSi10Mg composites: a comparative study on Gd_2O_3 and Er_2O_3 additions. Mater Charact. 2022b;192:112206.

[3] Jandaghi MR, Aversa A, Mabfredi D, et al. In situ alloying of AlSi10Mg-5wt% Ni through laser powder bed fusion and subsequent heat treatment. J Alloys Compd. 2022c;904:164081.

[4] Wang JY, Gao JB, Yang HL, et al. High-strength Al-5Mg2Si-2Mg-2Fe alloy with extremely high Fe content for green industrial application through additive manufacturing. Virtual Phys Prototyp. 2023a;18:2235587.

[5] Wang QZ, Kang N, Lin X, et al. High strength Al-Cu-Mg based alloy with synchronous improved tensile properties and hot-cracking resistance suitable for laser powder bed fusion. J Mater Sci Technol. 2023b;141:155–170.

[6] Wang QZ, Kang N, Lin X, EL Mansori M, Liu Y, Lu JL, Wang YF, Chai HZ, Huang WD. On the Si-induced microstructure evolution, solidification cracking healing and strengthening behavior of laser powder bed fusion additive manufactured Al-Cu-Mg/Si alloys. J Mater Process Technol. 2023c;313:117860.

[7] Yang FP, Wang JY, Wen T, et al. Double-peak age strengthening of an Al-Mg-Si-Zn alloy processed by laser powder bed fusion. J Mater Sci Technol. 2024;192:82–94.

[8] Wen T, Wang JY, Li ZC, et al. Microstructural evolution and strengthening mechanisms of a high-strength Al-Mg-Si alloy processed by laser powder bed fusion and ageing treatment. Mater Charact. 2024;209:113754.

[9] Wang JY, Yang FP, Yang HL, et al. Effect of heat treatment on the microstructure and mechanical properties of an Al-5Mg2Si-2Mg alloy processed by laser powder bed fusion. J Alloys Compd. 2022;920:165944.

[10] Aboulkhair NT, Simonelli M, Parry L, et al. 3D printing of aluminium alloys: additive manufacturing of aluminium alloys using selective laser melting. Prog Mater Sci. 2019;106:100578.

[11] Yang FP, Wang JY, Wen T, et al. Manipulating microstructure and mechanical properties of laser powder bed fusion processed hypo-eutectic Al-13.3Mg2Si alloy via annealing. J Alloys Compd. 2023;967:171805.

[12] Liu JW, Kou S. Susceptibility of ternary aluminum alloys to cracking during solidification. Acta Mater. 2017;125:513–523.

[13] Tan QY, Zhang JQ, Sun Q, et al. Inoculation treatment of an additively manufactured 2024 aluminium alloy with titannium nanoparticles. Acta Mater. 2020;196:1–16.

[14] Li G, Huang YH, Li XW, et al. Laser powder bed fusion of nano-titania modified 2219 aluminium alloy with superior mechanical properties at both room and elevated

temperatures: the significant impact of solute. Addit Manuf. 2022;60:103296.

[15] Kou S. A criterion for cracking during solidification. Acta Mater. 2015;88:366–374.

[16] Li WZ, Qian F, Li JY, et al. Design strategy for eliminating cracking and improving mechanical properties of Al-Mg-Si alloys fabricated by laser melting deposition. Addit Manuf. 2023;68:103513.

[17] Sonawane A, Roux G, Blandin J-J, et al. Cracking mechanism and its sensitivity to processing conditions during laser powder bed fusion of a structural aluminum alloy. Materialia. 2021;15:100976.

[18] Kaufmann N, Imran M, Wischeropp TM, et al. Influence of process parameters on the quality of aluminium alloy EN AW 7075 using selective laser melting (SLM). Phys Procedia. 2016;83:918–926.

[19] Zhu ZG, Hu ZH, Ng FL, et al. Extending the mechanical property regime of laser powder bed fusion Sc- and Zr-modified Al6061 alloy by manipulating process parameters and heat treatment. Addit Manuf. 2024;85:104164.

[20] Oko O, Mbakaan C, Barki E. Experimental investigation of the effect of processing parameters on densification, microstructure and hardness of selective laser melted 7075 aluminium alloy. Mater Res Express. 2020;7:036512.

[21] Uddin SZ, Espalin D, Mireles J, Morton P, Terrazas C, Collins S, Murr LE, Wicker R. Laser powder bed fusion fabricated and characterization of crack-free aluminum alloy 6061 using in-process powder Bed induction heating. In: *International Solid Freeform Fabrication Symposium, University of Texas at Austin*; 2017.

[22] Uddin SZ, Murr LE, Terrazas CA, et al. Processing and characterization of crack-free aluminum 6061 using high temperature heating in laser powder bed fusion additive manufacturing. Addit Manuf. 2018;22:405–415.

[23] Mehta A, Zhou L, Huynh T, et al. Additive manufacturing and mechanical properties of the dense and crack free Zr-modified aluminum alloy 6061 fabricated by the laser-powder bed fusion. Addit Manuf. 2021;41:101966.

[24] Qbau N, Nam N, Ca N, et al. The crack healing effect of scandium in aluminum alloys during laser additive manufacturing. J Manuf Process. 2020;50:241–246.

[25] Martin JH, Yahata BD, Hundley JM, et al. 3D printing of high-strength aluminium alloys. Nature. 2017;549:365–369.

[26] Opprecht M, Garandet JP, Roux G, et al. A solution to the hot cracking problem for aluminium alloys manufactured by laser beam melting. Acta Mater. 2020;197:40–53.

[27] Opprecht M, Garandet JP, Roux G, et al. An understanding of duplex microstructures encountered during high strength aluminium alloy laser beam melting processing. Acta Mater. 2021;215:117024.

[28] Zhang JL, Gao JB, Song B, et al. A novel crack-free Ti-modified Al-Cu-Mg alloy designed for selective laser melting. Addit Manuf. 2021;38:101829.

[29] Wen T, Li Z, Wang J, et al. From crack-prone to crack-free: eliminating cracks in additive manufacturing of high-strength Mg_2Si-modified Al-Mg-Si alloys. J Mater Sci Technol. 2025;204:276–291.

[30] Ryen Ø, Holmedal B, Nijs O, et al. Strengthening mechanisms in solid solution aluminum alloys. Metallurgical and Materials Transactions A. 2006;37:1999–2006.

[31] Quested TE, Dinsdale AT, Greer AL. Thermodynamic modelling of growth restriction effects in aluminium alloys. Acta Mater. 2005;53:1323–1334.

[32] Rappaz M, Drezet JM, Gremaud M. A new hot-tearing criterion. Metall Mater Trans A. 1999;30:449–455.

[33] Otani Y, Sasaki S. Effects of the addition of silicon to 7075 aluminum alloy on microstructure, mechanical properties, and selective laser melting processability. Mater Sci Eng A. 2020;777:139079.

[34] Tan QY, Fan ZQ, Tang XQ, et al. A novel strategy to additively manufacture 7075 aluminium alloy with selective laser melting. Mater Sci Eng A. 2021;821:141638.

[35] Committe, ASM. Properties and Selection: Nonferrous Alloys and Special-Purpose Materials. Metals Handbook; 1990.

[36] Maamoun AH, Xue YF, Elbestawi MA, et al. The effect of selective laser melting process parameters on the microstructure and mechanical properties of Al6061 and AlSi10Mg alloys. Materials (Basel). 2019;12:12.

[37] Kimura T, Nakamoto T. Microstructures and mechanical properties of A356 (AlSi7Mg0.3) aluminum alloy fabricated by selective laser melting. Mater Des. 2016;89:1294–1301.

[38] Rao JH, Zhang Y, Zhang K, et al. Selective laser melted Al-7Si-0.6Mg alloy with in-situ precipitation via platform heating for residual strain removal. Mater Des. 2019;182:108005.

[39] Ming XL, Song D, Yu A, et al. Effect of heat treatment on microstructure, mechanical and thermal properties of selective laser melted AlSi7Mg alloy. J Alloys Compd. 2023;945:169278.

[40] Xiong ZH, Liu SL, Li SF, et al. Role of melt pool boundary condition in determining the mechanical properties of selective laser melting AlSi10Mg alloy. Mater Sci Eng A. 2019;740–741:148–156.

[41] Amani Y, Dancette S, Delroisse P, et al. Compression behavior of lattice structures produced by selective laser melting: X-ray tomography based experimental and finite element approaches. Acta Mater. 2018;159:395–407.

[42] Girelli L, Tocci M, Gelfi M, et al. Study of heat treatment parameters for additively manufactured AlSi10Mg in comparison with corresponding cast alloy. Mater Sci Eng A. 2019;739:317–328.

[43] Saha S, Todorova TZ, Zwanziger JW. Temperature dependent lattice misfit and coherency of Al_3X (X = Sc, Zr, Ti and Nb) particles in an Al matrix. Acta Mater. 2015;89:109–115.

[44] Li RD, Wang MB, Li ZM, et al. Developing a high-strength Al-Mg-Si-Sc-Zr alloy for selective laser melting. Acta Mater. 2020;193:83–98.

[45] Li GC, Brodu E, Soete J, et al. Exploiting the rapid solidification potential of laser powder bed fusion in high strength and crack-free Al-Cu-Mg-Mn-Zr alloys. Addit Manuf. 2021;47:102210.

[46] Yang FP, Wang JY, Wen T, et al. Developing a novel high-strength Al–Mg–Zn–Si alloy for laser powder bed fusion. Mater Sci Eng A. 2022;851:143636.

[47] Herzog D, Seyda V, Wycisk E, et al. Additive manufacturing of metals. Acta Mater. 2016;117:371–392.

[48] Prasad A, Yuan L, Lee P, et al. Towards understanding grain nucleation under additive manufacturing solidification conditions. Acta Mater. 2020;195:392–403.

[49] Hu L, Li Y, Luo GD, et al. Understanding cellular structure formation in rapidly solidified Al–Ni alloys by constructing solidification microstructure selection maps. Addit Manuf. 2023;73:103671.

[50] Zhu XZ, Yang HL, Dong XX, et al. The effects of varying Mg and Si levels on the microstructural inhomogeneity and eutectic Mg_2Si morphology in die-cast Al-Mg-Si alloys. J Mater Sci. 2018;54: 5773–5787.

[51] Czerwinski F. The growth of quaternary divorced eutectic in Al-Ce-Si-Mg alloys. Metall Mater Trans A. 2023;54:391–398.